

Reconstruction of Three-dimensional Scroll Wave Chaos in Opaque and Transparent Excitable Media using Deep Neural Networks

Jan Lebert, Meenakshi Mittal, and Jan Christoph*

Cardiovascular Research Institute, University of California, San Francisco, USA

(Dated: September 16, 2022)

Scroll wave chaos is thought to underlie life-threatening ventricular fibrillation. However, currently there is no direct way to measure action potential wave patterns transmurally throughout the thick ventricular heart muscle. Consequently, direct observation of three-dimensional electrical scroll wave chaos remains elusive. Here, we study whether it is possible to reconstruct simulated three-dimensional scroll wave chaos inside a bulk-shaped excitable medium from two-dimensional observations of the wave dynamics on the bulk's surface using deep learning. We trained encoding-decoding convolutional neural networks to predict three-dimensional scroll wave chaos inside opaque and transparent as well as isotropic and anisotropic excitable media from two-dimensional projections or observations of the wave dynamics on the surface. We tested whether observations from one or two opposing surfaces would be sufficient, whether incorporating measurements of the surface deformation improves the reconstruction, and tested the feasibility of predicting the bulk's thickness. We demonstrate that it is possible to fully reconstruct three-dimensional scroll wave chaos in transparent excitable media with anisotropy and to obtain partial reconstructions in opaque excitable media when analyzing two opposing layers of the bulk. We found that anisotropy provides crucial information for neural networks to decode depth, which facilitates the reconstructions. In the future, deep neural networks could be used to visualize transmural action potential wave patterns during ventricular fibrillation from epi- or endocardial recordings.

Keywords: Scroll waves, excitable media, action potential waves, ventricular fibrillation, deep learning

I. INTRODUCTION

Scroll wave chaos occurs in excitable reaction-diffusion systems, termed 'excitable media', and is thought to underlie ventricular fibrillation. In the heart, nonlinear waves of electrical excitation or action potential waves propagate through the cardiac muscle and initiate its contractions. The electrical waves are conjectured to degenerate into electrical scroll wave chaos via a cascade of wavebreaks during the onset of ventricular fibrillation. However, direct evidence for the existence of scroll wave chaos in the heart is lacking. While the dynamics of scroll wave chaos have been studied extensively in computer simulations [1, 2], it remains a challenge to directly visualize scroll wave chaos throughout the depths of the heart muscle.

Spiral wave-like vortex-shaped action potential waves can be imaged on the heart surface during ventricular tachycardia or fibrillation using voltage-sensitive optical mapping [3–7]. The surface observations are in agreement with simulated three-dimensional scroll wave dynamics in realistic simulations [2]. Otherwise, only few and indirect experimental evidence of scroll waves during ventricular fibrillation exists. Voltage-sensitive transillumination imaging was used to measure projections of scroll waves on the surface of the isolated right ventricle of porcine and sheep hearts [8–10]. The right ventricles are thinner than the left and can therefore be penetrated, to a certain extent (~ 0.5 cm), by near-infrared

light. With the approach it is possible to locate focal wave sources inside the volume of the right ventricle [11, 12]. More recently, it was shown that ultrasound imaging can reveal mechanical vortices in the ventricles of whole isolated porcine hearts, which co-exist with electrical vortices on the epicardial surface, suggesting that the heart's mechanical dynamics reflect electrical scroll wave dynamics [6, 13]. However, it remains difficult to extrapolate the measured projections or surface observations of the electrical dynamics into the depths of the cardiac muscle, and eventually correlate them with mechanical measurements. Fully three-dimensional reconstructions of scroll waves were obtained using optical tomography in the Belousov-Zhabotinsky chemical reaction, which is a transparent excitable medium exhibiting very similar wave phenomena as cardiac tissue [14–17]. In contrast, three-dimensional action potential waves have been directly measured in small rat and zebrafish hearts using laminar optical tomography [18] or light-sheet microscopy [19]. However, attempts to obtain three-dimensional visualizations of scroll waves inside the optically dense cardiac muscle of large mammalian hearts have not yet attained a similar quality, and better measurement and reconstruction techniques are needed.

Multiple numerical approaches for the reconstruction of scroll waves from surface observations have previously been proposed: Berg et al. [20] attempted to recover simulated scroll wave chaos from single-surface observations using a synchronization-based data-assimilation approach. However, while the approach was successful at recovering scroll wave chaos from sparse measurements within the medium, see also [21], it was not suited to extrapolate scroll wave dynamics into the three-

* <https://cardiacvision.ucsf.edu>; jan.christoph@ucsf.edu

dimensional bulk-shaped medium from surface observations. Hoffman et al. [22, 23] analyzed dual-surface observations (comparable to measuring both the epi- and endocard) using a different data-assimilation approach, the local ensemble transform Kalman filter [24], to successfully reconstruct individual simulated scroll waves including wavebreak with decent reconstruction error. The question remains if it is possible to reconstruct truly complex three-dimensional scroll wave chaos from single- or dual-surface observations. More recently, neural networks were used to predict cardiac dynamics from sparse or partial observations with promising results [25–27]. However, the task of predicting scroll wave dynamics from surface observations using neural networks has not yet been established.

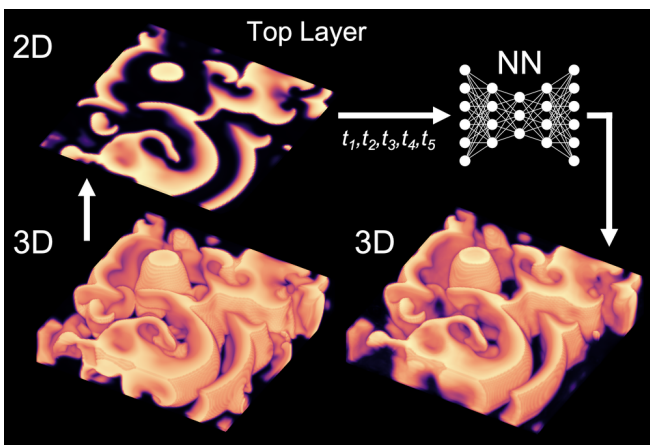


FIG. 1. Deep learning-based reconstruction of scroll wave chaos inside a three-dimensional volume from partial observations of the dynamics on its surface. Scroll wave chaos is a model for the electrophysiological dynamics underlying ventricular fibrillation. Computer simulations were performed in isotropic and anisotropic bulk-shaped excitable media. A neural network (NN) predicts scroll wave dynamics underneath the bulk’s surface from a short temporal sequence (t_1, \dots, t_5) of two-dimensional observations (here shown for top layer).

Here, we provide a numerical proof-of-principle that deep encoding-decoding convolutional neural networks, under certain conditions, can be used to reconstruct complex three-dimensional scroll wave chaos from two-dimensional observations of the dynamics on the surface of bulk-shaped excitable media. We show that scroll wave chaos can be recovered fully when analyzing projections of the three-dimensional dynamics on one surface of transparent anisotropic excitable media, and partially when analyzing two-dimensional wave patterns on two opposing surfaces of opaque isotropic or anisotropic excitable media. We tested several deep convolutional neural network architectures and analyzed their reconstruction performance depending on opacity, thickness and anisotropy of simulated excitable media.

II. METHODS

We simulated three-dimensional electrical scroll wave chaos in bulk-shaped isotropic and anisotropic excitable media with different thicknesses, and used neural networks to predict the three-dimensional wave patterns from a short sequence of two-dimensional observations of the dynamics on the bulk’s surface.

A. Scroll Wave Chaos in Elastic Excitable Media

We simulated electrical scroll wave chaos in bulk-shaped excitable media of size $128 \times 128 \times d_z$ voxels with varying thicknesses or depths $d_z \in \{8, 12, 16, 20, 24, 28, 32\}$. We used the phenomenological Aliev-Panfilov model [28] to simulate nonlinear waves of electrical excitation:

$$\frac{\partial u}{\partial t} = \nabla(\mathbf{D}\nabla u) - ku(u-a)(u-1) - ur \quad (1)$$

$$\frac{\partial r}{\partial t} = \epsilon(u, r)(ku(a+1-u) - r) \quad (2)$$

The dynamic variables u and r represent the local electrical excitation (voltage) and refractory state, respectively, and are dimensionless, normalized units. Together with the term $\epsilon(u, r) = \epsilon_0 + \mu_1 r / (u + \mu_2)$, the partial differential equations describe the local excitable kinetics and diffusive dynamics. The parameters $k = 8$, $a = 0.05$, $\epsilon_0 = 0.002$, $\mu_1 = 0.2$ and $\mu_2 = 0.3$ influence the properties of the excitation waves. The partial differential equations were integrated using the forward Euler method in a finite differences numerical integration scheme. We simulated both isotropic

$$\mathbf{D} = D_{\text{iso}}\mathbf{I} \quad (3)$$

and anisotropic excitable media with locally varying fiber direction with diffusion coefficients for the parallel D_{\parallel} and perpendicular D_{\perp} fiber direction:

$$\mathbf{D} = \begin{pmatrix} D_{11} & D_{12} & 0 \\ D_{21} & D_{22} & 0 \\ 0 & 0 & D_{33} \end{pmatrix} \quad (4)$$

$$D_{11} = D_{\parallel} \cos^2(\theta(z)) + D_{\perp} \sin^2(\theta(z))$$

$$D_{22} = D_{\parallel} \sin^2(\theta(z)) + D_{\perp} \cos^2(\theta(z))$$

$$D_{12} = D_{21} = (D_{\parallel} - D_{\perp}) \cos(\theta(z)) \sin(\theta(z))$$

$$D_{33} = D_{\perp}$$

Here, the fiber organization represents ventricular muscle tissue with muscle fibers aligned in sheets in the $x-y$ plane and the sheet-fiber orientation rotating throughout the thickness of the bulk. We used a varying fiber angle $\theta(z)$ ranging from 0° to 90° between the top and bottom layer of the bulk for the simulation depth $d_z = 24$ voxels:

$$\theta(z) = z \cdot \Delta\theta \quad (5)$$

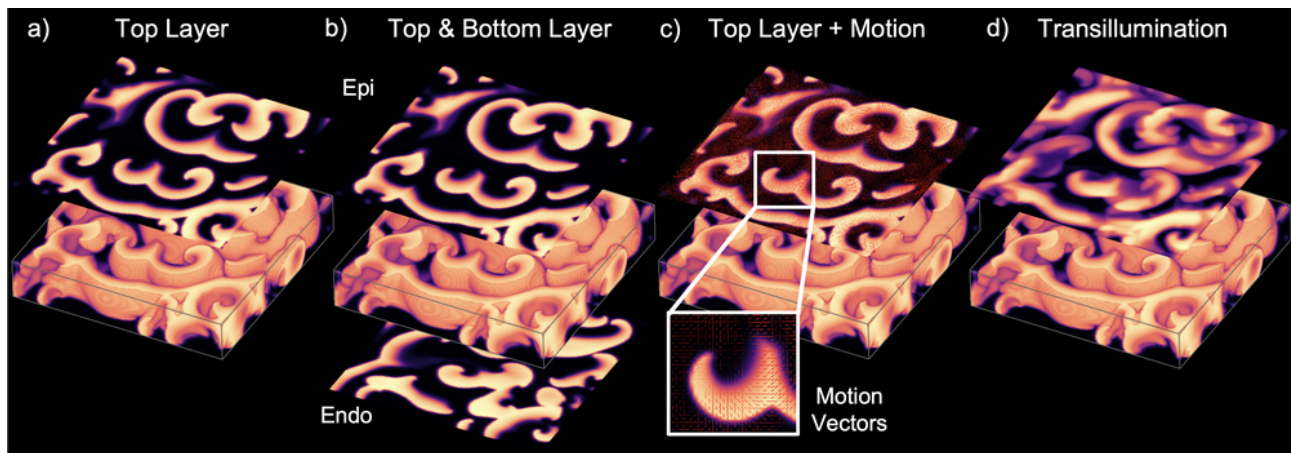


FIG. 2. Surface observations and projections of three-dimensional scroll wave chaos in a bulk medium. a) Observation of the top surface of the bulk (layer 1) in single-surface mode. b) Observation of the top and bottom surfaces of the bulk (layers 1 and 24) in dual-surface mode. c) Observation of the electrical activity and mechanical motion on the top surface of the bulk (layer 1) in single-surface mode (red: motion vectors). In a-c), the medium is opaque and does not allow observations of the dynamics inside the medium below the top layer. d) Observation of the projection (transillumination) of the three-dimensional dynamics along the depth of the bulk. The projection is calculated by summing the values in all 24 layers along the z -axis for a specific (x, y) -coordinate and dividing the sum by the number of layers. All layers 1 – 24 are cross-sections in the $x - y$ plane.

For the other depths, $d_z \in \{8, 12, 16, 20, 28, 32\}$, we used the same $\Delta\theta$ as in the $d_z = 24$ case. The ratio between the parallel D_{\parallel} and perpendicular D_{\perp} diffusion coefficients was set to 4 : 1. We chose $D_{\perp} = D_{\text{iso}} = 0.05$ and adapted the time between snapshots such that five snapshots correspond to about one spiral rotation period.

In addition to the purely electric simulations, we also simulated electromechanical scroll wave chaos in deforming excitable media, as described in [21]. Scroll wave chaos was initiated for all simulations by cross-field stimulation with added random noise to the bulk’s electrical potential. We performed 125 isotropic and anisotropic simulations for each depth, with 100 simulations being used for the training dataset and 25 simulations being exclusively used for evaluation. Each simulation contains 575 snapshots (approximately 115 spiral rotation periods) and we discarded the first 75 snapshots (15 spiral rotation periods) to obtain unique chaotic electrical states. The numerical simulation was implemented in C++, the source code for the simulations is available in [21].

B. Deep Learning-based Reconstruction of Scroll Wave Chaos

We implemented and tested deep neural networks, which each analyze a short temporal sequence of 5 subsequent two-dimensional snapshots of electrical wave patterns $\tilde{u}_t(x, y)$ to reconstruct a single fully three-dimensional snapshot $u_t(x, y, z)$ of scroll wave chaos:

$$(\tilde{u}_1(x, y), \dots, \tilde{u}_5(x, y)) \rightarrow u_1(x, y, z). \quad (6)$$

The two-dimensional snapshots, see Fig. 2, are either i) the top surface layer (single-surface mode):

$$\tilde{u}_t(x, y) = u_t(x, y, 1), \quad (7)$$

ii) both the top and bottom surface layer (dual-surface mode):

$$\tilde{u}_t(x, y) = (u_t(x, y, 1), u_t(x, y, d_z)), \quad (8)$$

iii) a projection of all u -values along the z -direction (depth) of the bulk:

$$\tilde{u}_t(x, y) = \frac{1}{d_z} \sum_{i=1}^{d_z} u_t(x, y, i), \quad (9)$$

or iv) both the electrical wave dynamics and the mechanical displacements $\vec{d} = (dx, dy)$ which occur in corresponding electromechanical simulations from the top surface layer (single-surface mode):

$$\tilde{u}_t(x, y) = (u_t(x, y, 1), dx(x, y, 1), dy(x, y, 1)). \quad (10)$$

The 5 snapshots were sampled over time and cover about one rotational period, similarly as described in [25] or [29]. For the top+bottom case (ii) and the mechanical displacement case (iv), we interleaved the snapshots.

We evaluated four different neural network architectures with basic and more intricate designs for the three-dimensional bulk prediction task (Eq. 6). While we primarily use a U-Net [30] architecture, we validate it against a simple encoder-decoder architecture, TransUNet [31] and MIRNet [32]. The encoder-decoder convolutional neural network (CNN) is similar to the architecture we previously used in [25, 29]. It consists of an encoder stage where the spatial resolution is progressively decreased, a latent space, and a decoder stage

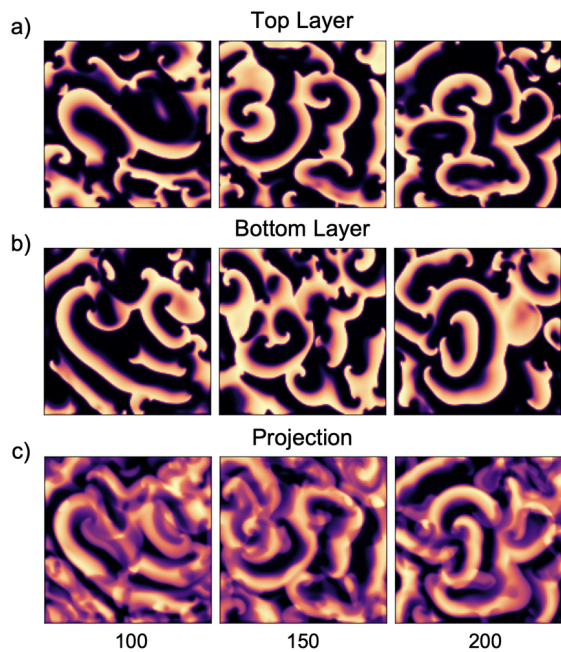


FIG. 3. Evolution of electrical scroll wave pattern as seen in the top layer, bottom layer and the projection of all 24 layers of a three-dimensional bulk with size $128 \times 128 \times 24$ voxels. The top and bottom layers are dissociated suggesting that the dynamics are three-dimensional. The projection is calculated for a given (x, y) -coordinate by averaging the u -values ($u \in [0, 1]$) along the z -direction or depth of the bulk. Time units in number of snapshots.

where the spatial resolution is progressively increased back to the original resolution. The encoding and decoding steps consist of three steps, in each two padded two-dimensional convolutional layers (2D-CNN) with filter size 3×3 and rectified linear unit [33] (ReLU) activation are applied, followed by batch normalization [34] and maxpooling (encoder) or upscaling (decoder), respectively. The U-Net architecture is identical to the encoder-decoder CNN architecture, except that skip connections are added between the encoder and decoder stages (see [30]). The TransUNet combines the U-Net architecture with self-attention mechanisms of Transformers [35] in its the latent space. The MIRNet architecture is different from the other evaluated architectures, as it contains parallel multi-resolution branches with information exchange, as well as spatial and channel attention mechanisms [32]. It aims at maintaining spatially-precise high-resolution representations through the entire network, while simultaneously receiving strong contextual information from the low-resolution representations. For all neural network architectures we use the generalized Charbonnier loss function [36, 37]:

$$l(u, \hat{u}) = \sqrt{(\hat{u} - u)^2 + \epsilon^2}, \quad (11)$$

where u is the three-dimensional ground truth, \hat{u} the prediction and we choose $\epsilon = 0.001$. The Charbonnier loss function behaves like L2 loss (mean squared error) when

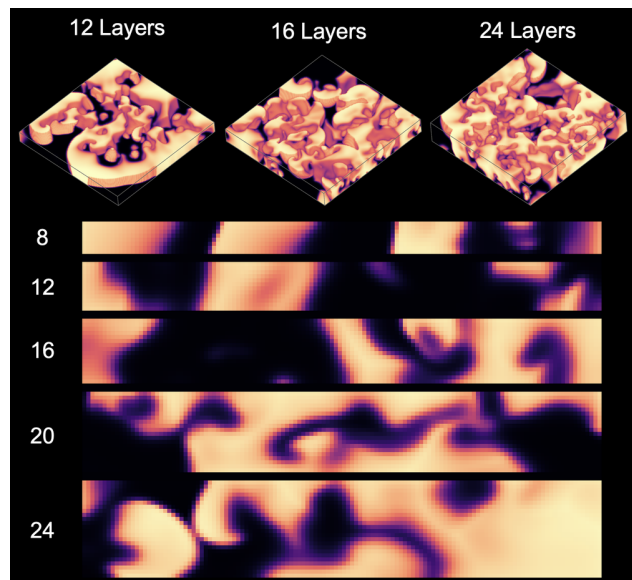


FIG. 4. Bulk thickness and transmurality of scroll wave dynamics. Scroll wave chaos with different bulk thicknesses $d_z = \{8, 12, 16, 20, 24\}$, also shown in corresponding cross-sections. The dynamics are quasi two-dimensional with $d_z = 8$. Dissociation between top and bottom layers starts to emerge at $d_z = 12$ as the dynamics become increasingly three-dimensional. At $d_z > 12$ the dynamics are fully three-dimensional.

$u \approx \hat{u}$ and like L1 loss (mean absolute error) otherwise. Using the simulated data described in section II A, we generated 20,000 training samples from the 100 training simulations for each depth d_z for both isotropic and anisotropic simulations. Similarly we created a separate evaluation dataset of 5,000 samples from the 25 evaluation simulations for each depth d_z . We evaluated the accuracy of the predictions on the evaluation datasets with the root mean squared error (RMSE) on each z -axis layer:

$$\text{RMSE}(z) = \sqrt{\frac{1}{N} \sum_{x,y,t} (\hat{u}(x, y, z, t) - u(x, y, z, t))^2} \quad (12)$$

To validate our findings, we studied if a neural network can accomplish a simpler task than the three-dimensional prediction: estimate the depth d_z of the simulation bulk from 5 two-dimensional observations. We tested both a depth regression and a depth classification neural network, which each predict the depth d_z of the simulation bulk

$$(\tilde{u}_1(x, y), \dots, \tilde{u}_5(x, y)) \rightarrow d_z. \quad (13)$$

The depth regression network predicts the depth d_z as a continuous value, while the depth classification network predicts the depth d_z as one of $\{8, 12, 16, 20, 24, 28, 32\}$. For this task we used the encoder part from the encoder-decoder architecture, followed by a global average pooling layer, two dense layers with 1024 filters with batch nor-

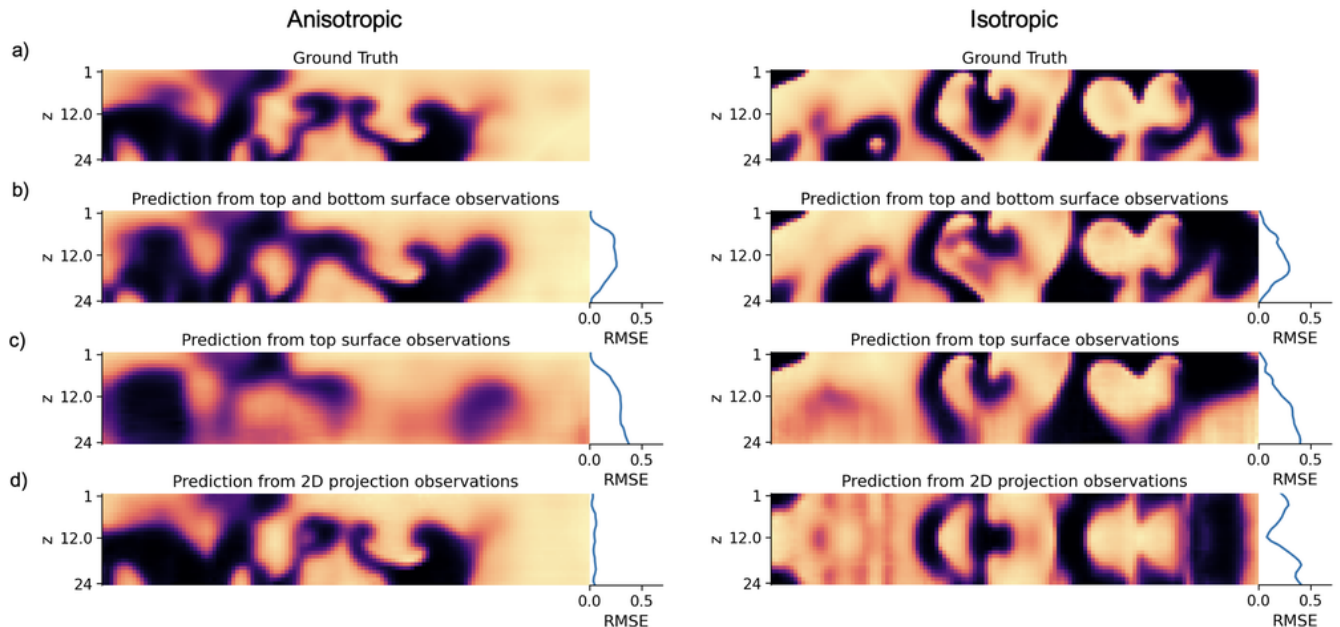


FIG. 5. Predictions of electrical excitation waves in subsurface layers of anisotropic (left) and isotropic (right) bulk tissue with dimension $128 \times 128 \times 24$ voxels. Scroll wave chaos shown in cross-sections which intersect the bulk at its center. a) Ground-truth scroll wave dynamics (representative snapshots) b) Prediction in dual-surface mode analyzing the top and bottom layers of an opaque bulk tissue. c) Prediction in single-surface mode analyzing the top surface layer of an opaque bulk. d) Prediction analyzing the z -projection of the dynamics along its depth (or z -axis) in a transparent bulk. The depth-profile of the prediction error (RMSE: root mean squared error) along the z -axis is shown to the right of each prediction. The reconstruction is successful in anisotropic transparent media, but fails in isotropic transparent media, as shown in d). In opaque media, the reconstruction performs sufficiently well in dual-surface mode with larger errors emerging at the center of the bulk, as shown in b). In transparent isotropic media, the subsurface prediction fails because the network is unable to infer the depth of the layers.

malization and ReLU activation, and ultimately an output dense layer with one filter (for regression) or seven filters (for classification). For the depth classification neural network we used a categorical cross-entropy loss function with a softmax activation function for the last layer, and for the depth regression network mean squared error as loss function and ReLU as activation function. The datasets for the depth estimation was generated from the bulk prediction task datasets. We used 4,000 random samples for each depth for the training dataset and 500 samples for the evaluation dataset (in total 28,000 training samples and 3,000 evaluation samples).

The networks were trained using the Adam [38] optimizer with a learning rate of 10^{-3} for the bulk prediction tasks and 10^{-5} for the depth regression and classification task for 20 epochs. We use a batch size of 32 for the Encoder-Decoder and U-Net architectures and a batch size of 4 for TransUNet and MIRNet. All neural network models were implemented in Tensorflow [39] using Keras [40]. Training and reconstructions were performed on NVIDIA RTX A5000 graphics processing units (GPUs).

Model	Parameters	Training Time
Encoder-Decoder	6,829,309	44 min
U-Net	8,278,168	55 min
TransUNet	406,899,608	19 hours
MIRNet	145,358,026	17 hours
d_z Regression	426,593	5 min
d_z Classification	432,743	5 min

TABLE I. Different neural network architectures used in this study and their respective number of trainable parameters and training times for 20 epochs. Training was performed on a single NVIDIA RTX A5000 GPU.

III. RESULTS

Using deep convolutional neural networks, it is possible to accurately and fully reconstruct three-dimensional scroll wave chaos in transparent anisotropic excitable media and to partially reconstruct three-dimensional scroll wave chaos in opaque excitable media, see Figs. 5-7. In opaque excitable media, the reconstruction accuracy improves if i) the two opposing top and bottom surface layers are analyzed and ii) the scroll wavelength is not much shorter than the thickness d_z of the bulk.

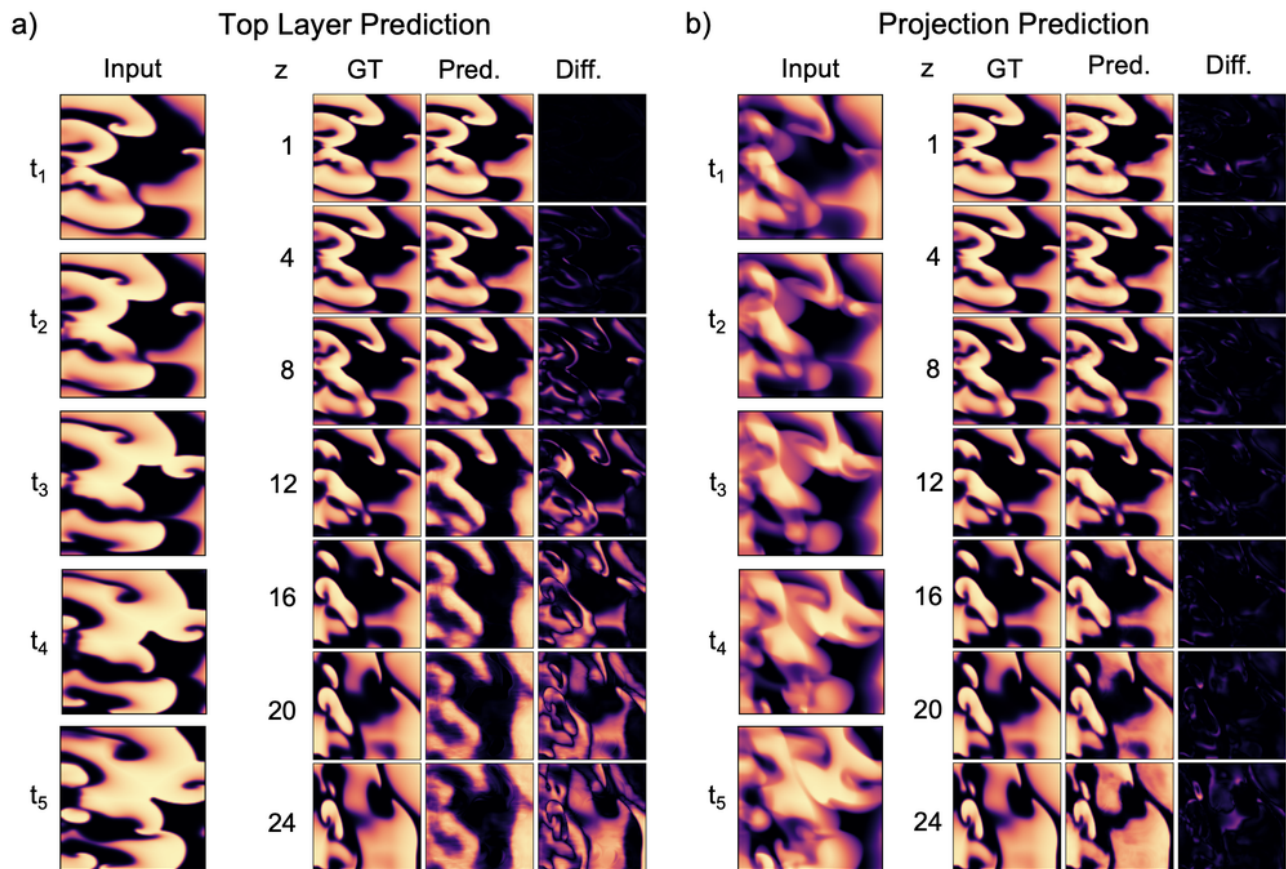


FIG. 6. Predictions of electrical excitation waves in subsurface layers of a bulk-shaped excitable medium with rotating laminar anisotropy from observing either a) the top layer of the bulk or b) the projection of the three-dimensional wave pattern in a transparent bulk along its depth (or z -axis). The bulk's dimensions are $128 \times 128 \times 24$ voxels. Predictions are shown for the 24 layers along the z -axis of the bulk, where the first layer is the top layer and the 24th layer is the bottom layer. First row: The five two-dimensional frames (t_1, \dots, t_5) which are the input for the neural network prediction. Second row: Ground truth (GT) electrical excitation wave pattern within cross-sectional layers (1-24), of which layers 2-24 cannot be observed. Note that the pattern changes from layer to layer throughout the bulk. Third row: Prediction of the current cross-sectional layer (1-24) by the neural network. Fourth row: Absolute difference per voxel between prediction and ground-truth.

A. Transparent vs. Opaque Excitable Media

Figs. 5 and 6 show a comparison of cross-sections of the three-dimensional scroll wave dynamics reconstructed from two-dimensional observations of the dynamics in opaque and transparent excitable media, respectively. The average prediction error along the depth in terms of the root mean squared error (RMSE) over the whole evaluation datasets are shown in Fig. 7 for $d_z \in \{8, 12, 16, 20, 24, 28, 32\}$. The input of the neural networks are 5 temporal snapshots covering approximately one spiral rotation period sampled from either the

- top surface in an opaque medium (Fig. 5c, 6a, 7a)
- top and bottom surface in an opaque medium (Fig. 5b, 7b)
- projection in a transparent medium along its depth

by observing the mean of all u -values along the z -axis (Fig. 5d, 6b, 7c).

For each case we trained a separate neural network with U-Net architecture. Fig. 5 shows cross-sections along the depth of the bulk (z -direction) and Fig. 6 shows cross-sections parallel to the surface in the x - y plane of the bulk. For opaque excitable media with top surface observations (both isotropic and anisotropic), the network is able to predict the first layers sufficiently well, but tends to miss finer structures at deeper layers and eventually fails to make accurate predictions in the second half of the bulk, see Figs. 5c) and 6a). At deeper locations, the network tends to replicate the dynamics from the layers at midwall in subsequent layers. Due to the chaotic nature of the dynamics, the surface and the predictions in deeper layers become quickly uncorrelated, which suggests that the network does not have enough information about the dynamics by simply analyzing them at the top layer. However, disregarding smaller features, the initial

2 – 8 layers in Figs. 5c) and 6a) are reconstructed sufficiently well. Panels a) and b) in Fig. 7 show a linear increase of the root mean squared error (RMSE) with increasing depths to about $z = 10 - 20$ layers, where afterwards the error saturates between 0.3 and 0.4. With thin bulks with depths $d_z = 8$, as shown on the top left in Fig. 4, the error remains small (< 0.1), likely because the dynamics are still quasi-two-dimensional. All errors were calculated by averaging the errors in all voxels over the evaluation dataset.

If the network analyzes two opposing surfaces of the bulk in dual-surface mode, as shown in Fig. 2b), the prediction accuracy becomes overall better, but also behaves similarly as in single-surface mode, see Figs. 5b) and 7b). Again, the prediction error increases steeply and linearly from both sides as the network tries to predict deeper into the bulk. However, overall, the maximal prediction error, which now occurs at the center of the bulk, is slightly lower as the maximal prediction error "on the other side" of the bulk in single-surface mode, see Fig. 7b). In both single- and dual-surface mode, the prediction performs similarly in isotropic or anisotropic excitable media. However, predictions are slightly better in thinner and slightly worse in thicker isotropic bulks than in anisotropic ones, respectively.

Lastly, the neural network is able to generate highly accurate predictions of the three-dimensional scroll wave chaos in transparent excitable media. More specifically, the neural network can provide predictions that are accurate transmurally, throughout the entire bulk, if the excitable medium is anisotropic. The left panel in Fig. 5d) and Fig. 6b) show cross-sections of three-dimensional predictions obtained in an anisotropic excitable medium, which match the ground-truth scroll wave pattern very closely. The root mean squared error (RSME) of the prediction is about 0.1 or less for various bulk depths ($d_z = 8 - 32$). However, as seen in the right panel in Fig. 5d), the prediction completely fails in isotropic transparent excitable media. Accordingly, the plots in Fig. 7 show that the prediction is only successful with anisotropy and not successful in isotropic excitable media. We describe the effect of the anisotropy in the next section in more detail.

B. Anisotropy

Ventricular muscle tissue is highly anisotropic due to the linearly transverse organization of cardiomyocytes and the presence of muscle fiber bundles, which are organized in sheets with the in-sheet orientation rotating throughout the depth of the ventricular wall (orthotropic organization). On the other hand, the Belousov-Zhabotinsky chemical reaction is an isotropic excitable medium. While both systems exhibit scroll waves, the scroll wave morphology can be very different in isotropic versus anisotropic media. In anisotropic excitable media, scroll waves are elongated in fiber direc-

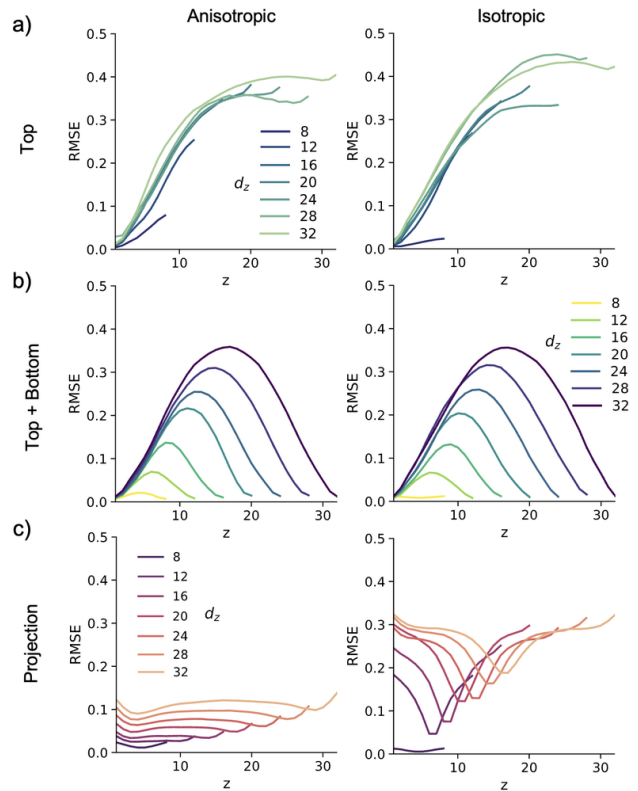


FIG. 7. Average prediction error (RMSE: root mean squared error) along z -axis in subsequent layers of a,b) opaque or c) transparent excitable media with or without anisotropy with bulk depths of $d_z \in \{8, 12, 16, 20, 24, 28, 32\}$ layers. a) Predictions in opaque media in single-surface mode analyzing 5 frames from the top surface with steep linear increase in the prediction error with both anisotropy and isotropy. b) Predictions in opaque media in dual-surface mode analyzing 5 frames from the top and bottom surfaces. The error increases linearly from both sides and reaches a maximum at midwall which increases with the thickness of the bulk. With opaque media, low errors are only obtained with dual-surface observations and quasi two-dimensional electrical dynamics with bulk depths of $d_z = 8, 12$. For opaque single- or dual-surface observations, we see no significant difference in the prediction accuracy between isotropic and anisotropic media. c) Predictions in transparent media using 5 projection frames. With anisotropy the error stays close to or below 0.1 RMSE, which corresponds to a mean absolute error (MAE) of about 5%. We trained separate U-Net neural networks for each combination.

tion as they propagate more quickly along this direction. The fiber orientation can often be recognized based on the action potential wave morphology on the ventricular surface of the heart during fibrillation in optical mapping recordings. Accordingly, in the simulated anisotropic bulk with the, for ventricular tissue typical, orthotropic rotating fiber organization, the waves are elongated differently at different depths, whereas in isotropic excitable media they are shaped similarly at all depths. It appears that the spatially nonuniform anisotropy enables the fully volumetric reconstruction in transparent anisotropic ex-

citable media, as shown in the left panel in Fig. 5, while in isotropic media the network cannot distinguish scroll waves closer to the surface from scroll waves deeper in the bulk, see also discussion. In isotropic transparent excitable media the network achieves good prediction accuracies at midwall, but performs poorly otherwise, see right panel in Fig. 7c). In opaque excitable media with single- or dual-surface observations, anisotropy does not alter the results significantly, as the reconstruction error is generally high and it is challenging to predict subsurface wave dynamics either way.

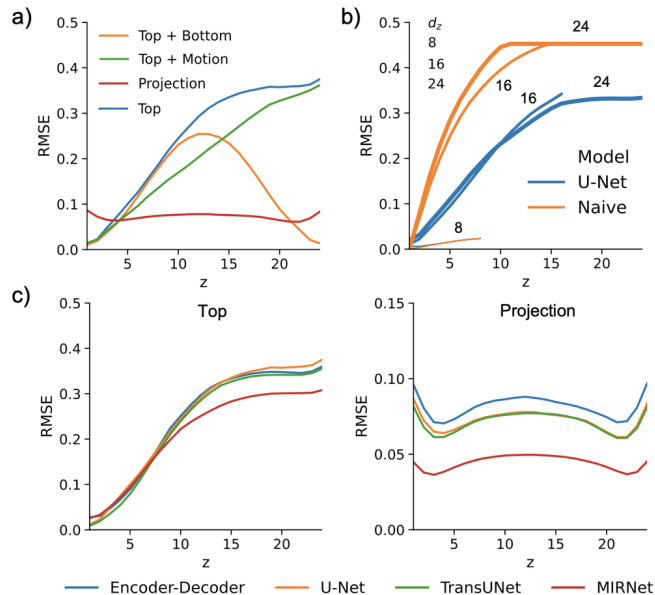


FIG. 8. Comparison of reconstruction errors (RMSE: root mean squared error) between different neural network architectures. a) Comparison of transmural reconstruction error along z -axis with single-surface observations analyzing the electrics on the top layer (blue), the electrics and motion on the top layer (green), electrics on both top and bottom layers (orange), and the z -projection of the three-dimensional electrics (red) for anisotropic media with $d_z = 24$. b) Comparison of reconstruction error for single-surface top layer predictions along z -axis obtained with U-Net (blue) vs. simple extrapolation (orange) repeating the top layer as $\hat{u}(x, y, z) = u(x, y, 1)$ in all subsequent layers in an isotropic medium with depths $d_z = 8, 16, 24$. c) Comparison of prediction error along z -axis obtained with different neural network architectures (Encoder-Decoder, U-Net, TransUNet, MIRNet) for both opaque and transparent anisotropic media with $d_z = 24$.

C. Network Types

We tested several deep neural network architectures (basic Encoder-Decoder, U-Net, TransUNet and MIRNet, see also section IIB) on the scroll wave prediction task and found that the prediction behavior is very similar across the different architectures, see Fig. 8c) and d). We observed that the MIRNet architecture produces the

lowest reconstruction error, while Encoder-Decoder, U-Net, and TransUNet all have similar but slightly higher reconstruction errors. In opaque excitable media, the prediction error (RMSE: mean root squared error) rises linearly and steeply with deeper layers equally with all networks, as seen for the single-surface reconstructions shown in the left panel in Fig. 8c) for anisotropic scroll wave chaos in a bulk with thickness $d_z = 24$. The prediction error saturates equally with all networks at depths $d_z > 10$ where they produce maximal prediction errors of about 0.3 (RMSE). MIRNet provides a slightly lower maximal error than the other networks. All networks achieve small prediction errors of < 0.1 (RMSE) in transparent excitable media with anisotropy, as seen for the projection reconstructions shown in the right panel in Fig. 8c) for anisotropic scroll wave chaos in a bulk with thickness $d_z = 24$. MIRNet provides the lowest error of less than 0.05 (RMSE), whereas the other networks produce errors ranging between 0.06 – 0.1 (RMSE). All networks produce the same characteristic error profile. Note that a RMSE of 0.1 corresponds to a mean absolute error (MAE) of about 5%. Therefore, all networks achieve reconstruction accuracies of greater than 95% in transparent excitable media. MIRNet even achieves reconstruction accuracies in the order of 97% – 98%.

As described in section IIB, U-Net differs from the Encoder-Decoder architecture in the inclusion of long skip connections, while TransUNet is a U-Net with a Transformer as the latent space. MIRNet is different in that it has multi-resolution branches with information exchange as well as self-attention mechanisms. The training times for 20 epochs and the number of trainable parameters for each network architecture are listed in Table I. Given that TransUNet and MIRNet provided either no or incremental improvements in prediction accuracy, while requiring significantly longer time to train, we primarily used U-Net in this study. U-Net required about an hour to train, while being competitive with the accuracy of MIRNet, which required almost a full day to train. All other results in Figs. 5-7 were obtained with the U-Net architecture, if not stated otherwise. We tested several U-Net sizes: a small model with 0.5M parameters, a medium network with 2M parameters and a large model with 8M parameters, determined that larger models perform better, and subsequently used the largest model. In some circumstances U-Net and TransUNet exhibited a significantly better reconstruction performance than the Encoder-Decoder network, but we did not observe significant differences in accuracy between U-Net and TransUNet.

D. Depth Estimation

It is possible to estimate the thickness or depth d_z of transparent bulks from projections of the corresponding scroll wave dynamics using either a regression or classification neural network. By contrast, it is not possible to

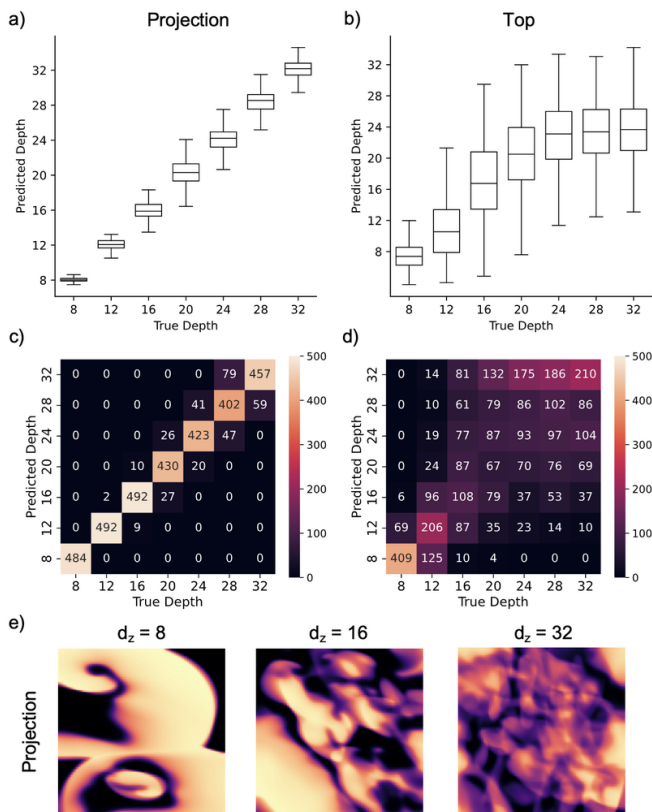


FIG. 9. Prediction of bulk thickness from surface observations of scroll wave chaos in a,c) transparent bulk medium with projection observations and b,d) opaque bulk medium with top surface observations using a) a regression or c,d) a classification neural network, respectively (all in anisotropic media). In transparent media, the thickness can be predicted from observations as shown in Fig. 3c), whereas in opaque media neither the regression nor classification neural networks predict the thickness correctly. e) Exemplary projection images for bulk thicknesses or depths $d_z = 8$, $d_z = 16$, and $d_z = 32$. Due to the averaging, the contrast of the waves decreases with increasing depths.

reliably predict the thickness of opaque bulks using either approach. Fig. 9a) shows predictions obtained with a regression neural network in transparent media. The regression neural network estimates the depth accurately with floating point precision (with a certain degree of uncertainty). Fig. 9c) shows a confusion matrix with depth predictions obtained with a classification neural network also in transparent media. The classification performs better than the regression. Out of ~ 500 predictions per thickness, only few attempts falsely classify the thickness (off-diagonal values). For both panels a) and c), predictions were made from two-dimensional observations as shown in Figs. 3c) and 9e). In particular, Fig. 9e) shows how the contrast of the waves decreases with increasing bulk thickness as more and more waves are superimposed and the signal is averaged along the z -axis. The neural network presumably associates the bulk's thickness with the contrast. Fig. 9b) shows predictions obtained with

a regression neural network in opaque media. The regression neural network does not predict the thickness or depth d_z correctly. Fig. 9d) shows predictions obtained with a classification neural network in opaque media. The classification neural network predicts random thicknesses and fails completely at correctly classifying the bulk's actual thickness. For both panels b) and d), predictions were made from two-dimensional observations as shown in Fig. 3a) or b). The data demonstrates that predicting the extent of scroll wave chaos is challenging with opacity, at least with our methodology. While scroll wave dynamics can vary qualitatively with different bulk thicknesses, in particular with thinner bulks, as shown in Figs. 4 and 5, there is a critical thickness beyond which the dynamics are dominated by the intrinsic excitable kinetics and are less influenced by the bulk's geometry and its boundaries. The heart muscle is not only opaque in the sense that it is hard to penetrate by light, but the scroll wave chaos itself is opaque in that it is difficult to compute scroll wave dynamics deeper in the heart wall behind a first layer of scroll waves.

IV. DISCUSSION

We demonstrated that deep neural networks can be used to reconstruct three-dimensional scroll wave chaos in transparent anisotropic excitable media as well as, with certain restrictions, in opaque excitable media. The reconstructions can be performed very efficiently within milliseconds on a graphics processing unit, and they do not require the collection of long time-series data, but succeed with a short series of images showing the three-dimensional wave dynamics on the surface of the excitable medium. Reconstructions can be performed particularly well in transparent and anisotropic excitable media, whereas reconstructions in opaque excitable media, in which only the surface data itself is available, are only moderately successful with accuracies dropping off quickly after about one scroll wavelength, see Figs. 5c), 6a) and 7b). We found this behaviour in opaque media with all the different neural network architectures that we tested. Given that the scroll wave dynamics are highly chaotic, and the dynamics visible in the top and bottom layers are completely dissociated, the partial reconstructions in opaque excitable media are yet a considerable result. In particular, if one assumes that there are unlikely more than two scroll wavelengths in the ventricle during ventricular fibrillation. In transparent excitable media, the results are poor with isotropy, but very good with anisotropy. Anisotropy is crucial because it implicitly encodes depth. The neural network learns to associate the alignment of the waves with the underlying fiber alignment which varies with depth. Moreover, it is able to decode this encoding even when multiple waves are superimposed in the projections, see Figs. 5d), 6b), 7c) and 9e) and Supplementary Video 1. Accordingly, the reconstruction fails in isotropic transparent excitable me-

dia as the network lacks depth information and it would equally fail in anisotropic excitable media with uniform linearly transverse anisotropy. Unfortunately, this means that the reconstruction approach is neither directly applicable to ventricular fibrillation, because the ventricular muscle is opaque, nor to the Belousov-Zhabotinsky reaction, which is transparent but isotropic. However, with near-infrared dyes and transillumination imaging, which allows imaging of action potential waves deeper inside the cardiac muscle, our approach could be applicable given that the muscle fiber architecture of the ventricular muscle allows for the depth encoding. Lastly, even without near-infrared dyes and superficial measurement data of action potential vortex waves on the surface of the heart, our approach is likely going to have practical relevance i) if dual-surface measurements from both the epi- and endocard are available, and ii) because the scroll wavelengths are likely not much shorter than the ventricular wall during ventricular fibrillation.

We have recently used similar encoding-decoding convolutional neural networks for the prediction of electrical scroll wave chaos from three-dimensional mechanical deformation [29], as well as for the prediction of phase maps and phase singularities from two-dimensional electrical spiral wave chaos [25]. While the networks performed very well in these applications, the results presented in this study are more sobering. Our study is another example of the more general notion that cardiac dynamics, and chaotic dynamics more generally, are challenging to predict [26, 41–45]. It is well known that classical deep learning approaches excel at interpolating, but do not perform well when aiming to extrapolate, which is what we aimed to do in this study. Therefore, the complete reconstruction of scroll wave chaos in opaque excitable media from surface observations alone will require a more

sophisticated approach.

V. CONCLUSIONS

We demonstrated that it is possible to reconstruct three-dimensional scroll wave chaos from two-dimensional observations using deep encoding-decoding neural networks. Reconstructions succeed under two conditions: either i) the medium is transparent and anisotropic with spatially varying anisotropy or ii) the medium is opaque and the dynamics are observed on two opposing surface layers while the scroll wavelength is not much shorter than the medium’s thickness. In the future, our methodology could be used to reconstruct transmural action potential wave dynamics during heart rhythm disorders such as ventricular fibrillation from epicardial or endocardial measurements.

VI. SUPPLEMENTARY MATERIAL

The Supplementary Videos can be found online at gitlab.com/janlebert/subsurface-supplementary-materials.

Supplementary Video 1: Neural network predictions of the full three-dimensional excitation from 5 two-dimensional projection frames for anisotropic medium with $d_z = 24$. The projection frame for each time point is shown on the left, the neural network prediction on the right. The true full three-dimension excitation is shown on the left in the second half of the video.

Supplementary Video 2: Comparison of the full three-dimensional neural network predictions from the top layer, top and bottom layer, or for the two-dimensional projection. The simulation is anisotropic and has a depth of 24 layers. In the second half of the video only the bottom 12 layers are visualized.

-
- [1] F. Fenton and A. Karma, Vortex dynamics in three-dimensional continuous myocardium with fiber rotation: Filament instability and fibrillation, *Chaos: An Interdisciplinary Journal of Nonlinear Science* **8**, 20 (1998).
 - [2] P. Pathmanathan and R. A. Gray, Filament dynamics during simulated ventricular fibrillation in a high-resolution rabbit heart, *BioMed Research International* **2015**, 10.1155/2015/720575 (2015).
 - [3] J. M. Davidenko, A. V. Pertsov, R. Salomonsz, W. Baxter, and J. Jalife, Stationary and drifting spiral waves of excitation in isolated cardiac muscle, *Nature* **355**, 349 (1992).
 - [4] A. M. Pertsov, R. Davidenko, J. M. Salomonsz, W. T. Baxter, and J. Jalife, Spiral waves of excitation underlie reentrant activity in isolated cardiac muscle, *Circulation Research* **72**, 631 (1993).
 - [5] A. Winfree, Electrical turbulence in three-dimensional heart muscle, *Science* **266**, 1003 (1994).
 - [6] J. Christoph, M. Chebbok, C. Richter, J. Schröder-Schetelig, P. Bittihn, S. Stein, I. Uzelac, F. H. Fenton, G. Hasenfuss, R. J. Gilmour, and S. Luther, Electromechanical vortex filaments during cardiac fibrillation, *Nature* **555**, 667 (2018).
 - [7] I. Uzelac, S. Iravani, N. K. Bhatia, and F. H. Fenton, Spiral wave breakup: Optical mapping in an explanted human heart shows the transition from ventricular tachycardia to ventricular fibrillation and self-termination, *Heart Rhythm* (2022).
 - [8] W. T. Baxter, S. F. Mironov, A. V. Zaitsev, J. Jalife, and A. M. Pertsov, Visualizing excitation waves inside cardiac muscle using transillumination, *Biophysical Journal* **80**, 516 (2001).
 - [9] O. Bernus, K. S. Mukund, and A. M. Pertsov, Detection of intramyocardial scroll waves using absorptive transillumination imaging, *Journal of Biomedical Optics* **12**, 014035 (2007).

- [10] B. G. Mitrea, M. Wellner, and A. M. Pertsov, Monitoring intramyocardial reentry using alternating transillumination, in *2009 Annual International Conference of the IEEE Engineering in Medicine and Biology Society* (2009) pp. 4194–4197.
- [11] V. D. Khait, O. Bernus, S. F. Mironov, and A. M. Pertsov, Method for the three-dimensional localization of intramyocardial excitation centers using optical imaging, *Journal of Biomedical Optics* **11**, 34007 (2006).
- [12] B. J. Caldwell, M. L. Trew, and A. M. Pertsov, Cardiac response to low-energy field pacing challenges the standard theory of defibrillation, *Circulation: Arrhythmia and Electrophysiology* **8**, 685 (2015).
- [13] A. Molavi Tabrizi, A. Mesgarnejad, M. Bazzi, S. Luther, J. Christoph, and A. Karma, Spatiotemporal organization of electromechanical phase singularities during high-frequency cardiac arrhythmias, *Phys. Rev. X* **12**, 021052 (2022).
- [14] B. J. Welsh, J. Gomatam, and A. E. Burgess, Three-dimensional chemical waves in the belousov–zhabotinskii reaction, *Nature* **304**, 611 (1983).
- [15] T. Bánsági and O. Steinbock, Three-dimensional spiral waves in an excitable reaction system: Initiation and dynamics of scroll rings and scroll ring pairs, *Chaos: An Interdisciplinary Journal of Nonlinear Science* **18**, 026102 (2008).
- [16] P. Dähmow, S. Alonso, M. Bär, and M. J. B. Hauser, Twists of opposite handedness on a scroll wave, *Phys. Rev. Lett.* **110**, 234102 (2013).
- [17] C. Bruns and M. J. B. Hauser, Dynamics of scroll waves in a cylinder jacket geometry, *Phys. Rev. E* **96**, 012203 (2017).
- [18] E. M. C. Hillman, O. Bernus, E. Pease, M. B. Bouchard, and A. Pertsov, Depth-resolved optical imaging of transmural electrical propagation in perfused heart, *Opt. Express* **15**, 17827 (2007).
- [19] L. Sacconi, L. Silvestri, E. C. Rodríguez, G. A. Armstrong, F. S. Pavone, A. Shrier, and G. Bub, KHz-rate volumetric voltage imaging of the whole zebrafish heart, *Biophysical Reports* **2**, 100046 (2022).
- [20] S. Berg, S. Luther, and U. Parlitz, Synchronization based system identification of an extended excitable system, *Chaos: An Interdisciplinary Journal of Nonlinear Science* **21**, 10.1063/1.3613921 (2011).
- [21] J. Lebert and J. Christoph, Synchronization-based reconstruction of electromechanical wave dynamics in elastic excitable media, *Chaos: An Interdisciplinary Journal of Nonlinear Science* **29**, 10.1063/1.5101041 (2019).
- [22] M. J. Hoffman, N. S. LaVigne, S. T. Scorse, F. H. Fenton, and E. M. Cherry, Reconstructing three-dimensional reentrant cardiac electrical wave dynamics using data assimilation, *Chaos: An Interdisciplinary Journal of Nonlinear Science* **26**, 013107 (2016).
- [23] M. J. Hoffman and E. M. Cherry, Sensitivity of a data-assimilation system for reconstructing three-dimensional cardiac electrical dynamics, *Philosophical Transactions of the Royal Society A: Mathematical, Physical and Engineering Sciences* **378**, 20190388 (2020).
- [24] B. R. Hunt, E. J. Kostelich, and I. Szunyogh, Efficient data assimilation for spatiotemporal chaos: A local ensemble transform kalman filter, *Physica D: Nonlinear Phenomena* **230**, 112 (2007), data Assimilation.
- [25] J. Lebert, N. Ravi, F. H. Fenton, and J. Christoph, Rotor localization and phase mapping of cardiac excitation waves using deep neural networks, *Frontiers in Physiology* **12**, 10.3389/fphys.2021.782176 (2021).
- [26] S. Herzog, R. S. Zimmermann, J. Abele, S. Luther, and U. Parlitz, Reconstructing complex cardiac excitation waves from incomplete data using echo state networks and convolutional autoencoders, *Frontiers in Applied Mathematics and Statistics* **6**, 10.3389/fams.2020.616584 (2021).
- [27] C. H. Martin, A. Oved, R. A. Chowdhury, E. Ullmann, N. S. Peters, A. A. Bharath, and M. Varela, EP-PINNs: Cardiac electrophysiology characterisation using physics-informed neural networks, *Frontiers in Cardiovascular Medicine* **8**, 10.3389/fcvm.2021.768419 (2022).
- [28] R. R. Aliev and A. V. Panfilov, A simple two-variable model of cardiac excitation, *Chaos, Solitons & Fractals* **7**, 293 (1996).
- [29] J. Christoph and J. Lebert, Inverse mechano-electrical reconstruction of cardiac excitation wave patterns from mechanical deformation using deep learning, *Chaos: An Interdisciplinary Journal of Nonlinear Science* **30**, 123134 (2020).
- [30] O. Ronneberger, P. Fischer, and T. Brox, U-net: Convolutional networks for biomedical image segmentation, in *Lecture Notes in Computer Science* (Springer International Publishing, 2015) pp. 234–241.
- [31] J. Chen, Y. Lu, Q. Yu, X. Luo, E. Adeli, Y. Wang, L. Lu, A. L. Yuille, and Y. Zhou, Transunet: Transformers make strong encoders for medical image segmentation, *CoRR abs/2102.04306* (2021), 2102.04306.
- [32] S. W. Zamir, A. Arora, S. Khan, M. Hayat, F. S. Khan, M.-H. Yang, and L. Shao, Learning Enriched Features for Real Image Restoration and Enhancement, in *Computer Vision – ECCV 2020*, Lecture Notes in Computer Science, edited by A. Vedaldi, H. Bischof, T. Brox, and J.-M. Frahm (Springer International Publishing, 2020) pp. 492–511.
- [33] V. Nair and G. E. Hinton, Rectified linear units improve restricted boltzmann machines (Omnipress, Madison, WI, USA, 2010) p. 807–814.
- [34] S. Ioffe and C. Szegedy, Batch normalization: Accelerating deep network training by reducing internal covariate shift, in *Proceedings of the 32nd International Conference on Machine Learning*, Proceedings of Machine Learning Research, Vol. 37, edited by F. Bach and D. Blei (PMLR, Lille, France, 2015) pp. 448–456.
- [35] A. Vaswani, N. Shazeer, N. Parmar, J. Uszkoreit, L. Jones, A. N. Gomez, L. Kaiser, and I. Polosukhin, Attention is all you need, in *Advances in Neural Information Processing Systems 30: Annual Conference on Neural Information Processing Systems 2017, December 4–9, 2017, Long Beach, CA, USA*, edited by I. Guyon, U. von Luxburg, S. Bengio, H. M. Wallach, R. Fergus, S. V. N. Vishwanathan, and R. Garnett (2017) pp. 5998–6008.
- [36] A. Bruhn, J. Weickert, and C. Schnörr, Lucas/Kanade meets Horn/Schunck: Combining local and global optic flow methods, *Int. J. Comput. Vis.* **61**, 211 (2005).
- [37] J. T. Barron, A General and Adaptive Robust Loss Function, in *2019 IEEE/CVF Conference on Computer Vision and Pattern Recognition (CVPR)* (2019) pp. 4326–4334.
- [38] D. P. Kingma and J. Ba, Adam: A method for stochastic optimization, in *3rd International Conference on Learning Representations, ICLR 2015, San Diego, CA, USA, May 7–9, 2015, Conference Track Proceedings*, edited by

Y. Bengio and Y. LeCun (2015).

- [39] M. Abadi, A. Agarwal, P. Barham, E. Brevdo, Z. Chen, C. Citro, G. S. Corrado, A. Davis, J. Dean, M. Devin, S. Ghemawat, I. Goodfellow, A. Harp, G. Irving, M. Isard, Y. Jia, R. Jozefowicz, L. Kaiser, M. Kudlur, J. Levenberg, D. Mané, R. Monga, S. Moore, D. Murray, C. Olah, M. Schuster, J. Shlens, B. Steiner, I. Sutskever, K. Talwar, P. Tucker, V. Vanhoucke, V. Vasudevan, F. Viégas, O. Vinyals, P. Warden, M. Wattenberg, M. Wicke, Y. Yu, and X. Zheng, TensorFlow: Large-scale machine learning on heterogeneous systems, <https://www.tensorflow.org> (2015).
- [40] F. Chollet *et al.*, Keras, <https://keras.io> (2015).
- [41] J. Pathak, B. Hunt, M. Girvan, Z. Lu, and E. Ott, Model-free prediction of large spatiotemporally chaotic systems from data: A reservoir computing approach, *Phys. Rev. Lett.* **120**, 024102 (2018).
- [42] J. Pathak, A. Wikner, R. Fussell, S. Chandra, B. R. Hunt, M. Girvan, and E. Ott, Hybrid forecasting of chaotic processes: Using machine learning in conjunction with a knowledge-based model, *Chaos: An Interdisciplinary Journal of Nonlinear Science* **28**, 041101 (2018).
- [43] S. Herzog, F. Wörgötter, and U. Parlitz, Data-driven modeling and prediction of complex spatio-temporal dynamics in excitable media, *Frontiers in Applied Mathematics and Statistics* **4**, 10.3389/fams.2018.00060 (2018).
- [44] S. Shahi, C. D. Marcotte, C. J. Herndon, F. H. Fenton, Y. Shiferaw, and E. M. Cherry, Long-time prediction of arrhythmic cardiac action potentials using recurrent neural networks and reservoir computing, *Frontiers in Physiology* **12**, 10.3389/fphys.2021.734178 (2021).
- [45] S. Shahi, F. H. Fenton, and E. M. Cherry, A machine-learning approach for long-term prediction of experimental cardiac action potential time series using an autoencoder and echo state networks, *Chaos: An Interdisciplinary Journal of Nonlinear Science* **32**, 063117 (2022).

VII. DATA AVAILABILITY STATEMENT

The data that support the findings of this study are available from the corresponding author upon reasonable request.

VIII. FUNDING

This research was funded by the University of California, San Francisco. The RTX A5000 GPUs used in this study were donated by the NVIDIA Corporation via the Academic Hardware Grant Program.

IX. AUTHOR CONTRIBUTIONS

JL and JC conceived the research and implemented the algorithms. JL, MM, and JC conducted the data analysis and designed the figures. JL and JC wrote the manuscript.

X. CONFLICT OF INTEREST

The authors declare that the research was conducted in the absence of any commercial or financial relationships that could be construed as a potential conflict of interest.